



**HAL**  
open science

**Explicit Computations and Further Extensive Simulations for Rigid-or Elastic-joint Arm: Technical Attachment to: " Aerial Robots with Rigid/Elastic-joint Arms: Single-joint Controllability Study and Preliminary Experiment " 2016 IEEE/RSJ International Conference on Intelligent Robots and Systems, Daejeon, South Korea, October 2016**

Burak Yüksel, Nicolas Staub, Antonio Franchi

► **To cite this version:**

Burak Yüksel, Nicolas Staub, Antonio Franchi. Explicit Computations and Further Extensive Simulations for Rigid-or Elastic-joint Arm: Technical Attachment to: " Aerial Robots with Rigid/Elastic-joint Arms: Single-joint Controllability Study and Preliminary Experiment " 2016 IEEE/RSJ International Conference on Intelligent Robots and Systems, Daejeon, South Korea, October 2016. [Technical Report] LAAS-CNRS; MPI - Max Planck Institute for Biological Cybernetics. 2016. hal-01345564v1

**HAL Id: hal-01345564**

**<https://hal.science/hal-01345564v1>**

Submitted on 14 Jul 2016 (v1), last revised 28 Jul 2016 (v2)

**HAL** is a multi-disciplinary open access archive for the deposit and dissemination of scientific research documents, whether they are published or not. The documents may come from teaching and research institutions in France or abroad, or from public or private research centers.

L'archive ouverte pluridisciplinaire **HAL**, est destinée au dépôt et à la diffusion de documents scientifiques de niveau recherche, publiés ou non, émanant des établissements d'enseignement et de recherche français ou étrangers, des laboratoires publics ou privés.

# Explicit Computations and Further Extensive Simulations for Rigid- or Elastic-joint Arm

Technical Attachment to:

## ”Aerial Robots with Rigid/Elastic-joint Arms: Single-joint Controllability Study and Preliminary Experiment” 2016 IEEE/RSJ International Conference on Intelligent Robots and Systems, Daejeon, South Korea, October 2016

Burak Yüksel<sup>1</sup>, Nicolas Staub<sup>2</sup> and Antonio Franchi<sup>2</sup>

**Abstract**—This document is a technical attachment to [1] that provides the explicit computations on the proofs and some numerical simulations. We also provide an informal recall of exact feedback linearization and differential flatness of the system at hand. In addition, Fig. 7 is given to support the experiment’s section of [1].

### I. ON EXACT INPUT-OUTPUT FEEDBACK LINEARIZATION VIA DYNAMIC FEEDBACK AND DIFFERENTIAL FLATNESS

In this section we informally recall some facts on exact feedback linearization and differential flatness, see [2], [3] for a thorough explanation. With reference to the system given in (1) of [1], let us consider a candidate output vector  $\mathbf{y}$  whose dimension is 3, as the input. We say that  $\mathbf{y}$  is differentially flat if the state  $\mathbf{q}, \dot{\mathbf{q}}$  of the system and the input  $\mathbf{u}$  can be written as an algebraic function of  $\mathbf{y}$  and a finite number of its derivatives. Flatness is a useful property for motion planning since one can plan in the lower-dimensional output space instead of planning for the full state.

On the other side, a system is exactly input-output linearizable with a dynamic feedback, if there exists a change of coordinates, possibly including a feedback input transformation, that brings the system in an equivalent linear and controllable form. A sufficient condition to obtain so is that if one derives w.r.t. time the components of  $\mathbf{y}$  until at least one input appears, the total relative degree matches with the dimension of the system state (taking into account possible additional integrators inserted in the input channels), hence no uncontrolled internal dynamics appears. This property is very useful for control purposes, in fact, if one rewrites the vector of derivatives of  $\mathbf{y}$  as  $\bar{\mathbf{y}}$ , one obtains

$$\bar{\mathbf{y}} = \bar{\mathbf{f}}(\bar{\mathbf{x}}) + \bar{\mathbf{G}}(\bar{\mathbf{x}})\bar{\mathbf{u}}, \quad (1)$$

<sup>1</sup>Max Planck Institute for Biological Cybernetics, Spemanstr. 38, 72076, Tübingen, Germany. burak.yueksel@tuebingen.mpg.de

<sup>2</sup>LAAS-CNRS, Université de Toulouse, CNRS, Toulouse, France, nstaub@laas.fr, afranchi@laas.fr

This work is partially funded by 1) the Eiffel Excellence Scholarship Programme by the French Ministry of Foreign Affairs and International Development, and by 2) the European Union’s Horizon 2020 research and innovation programme under grant agreement No 644271 AEROARMS.

where  $\bar{\mathbf{x}} \in \mathbb{R}^{\bar{n}}$  is the augmented state of dimension of  $\bar{n}$ , and  $\bar{\mathbf{G}}$  is an invertible decoupling matrix. Then the control law

$$\bar{\mathbf{u}} = \bar{\mathbf{G}}^{-1}(\mathbf{v} - \bar{\mathbf{f}}), \quad (2)$$

where  $\mathbf{v}$  is a virtual input, brings the system in the form

$$\dot{\bar{\mathbf{y}}} = \mathbf{v}, \quad (3)$$

which is linear and controllable, as long as  $\bar{\mathbf{G}}$  is invertible<sup>1</sup>. Once the system is transformed in form (3), any outer control loop for stabilizing linear systems can be used to design  $\mathbf{v}$ . Although both concepts sound different, differential flatness is equivalent to exact input-state linearizability via dynamic feedback in an open and dense set of the state space and an output is flat if and only if it is exactly linearizing [3]–[5]. Hence it is convenient to say that the exact linearizing outputs are flat outputs as well. Therefore in Sec. III and Sec. IV of [1] we used the feedback linearization method for controlling the system and also to find the differentially flat outputs. Moreover, in the following, we derive by inspection the algebraic map that relates the output to the state and the input.

We will now present sketches of the flatness proof for the case-R and case-E presented in [1].

#### A. Sketch of flatness part of the Proof of Proposition 1, Case-R

We recall the Proposition 1 (Case-R) of Sec. III of [1]:

**Proposition 1.** *The vector  $[\mathbf{p}_{c_1}^T \ \theta_{12}^T]^T$  is an exactly linearizing output via dynamic feedback for the model in Case-R, as long as  $u_i \neq 0$ . As a consequence, it is also a flat output.*

In order to possibly use the differential flatness for planning purposes, we sketch the procedure to explicitly write down the algebraic map that relates  $\mathbf{y}, \dot{\mathbf{y}}, \ddot{\mathbf{y}}, \mathbf{y}^{(3)}, \mathbf{y}^{(4)}$  with  $\theta_1, \dot{\theta}_1$ , and  $\mathbf{u}$ . In fact,  $\mathbf{p}_{c_1}$  and  $\theta_{12}$  are already part of  $\mathbf{y}$ . This procedure has been partially shown in [6] only in the special case that  $\mathbf{r}_G = \mathbf{0}$

<sup>1</sup>Notice that the equations equations (1–3) are identical to (2a), (2b) and (2c) of [1].

(i.e.,  $\mathbf{P}_{C1}$  and  $\mathbf{P}_G$  are coincident). The position of the CoM of overall system in  $\mathcal{F}_W$  is given by

$$\mathbf{p}_c = \frac{(m_1 + m_m)\mathbf{p}_{c1} + m_2\mathbf{p}_{c2}}{m_s}, \quad (4)$$

where  $\mathbf{p}_{c2} = \mathbf{p}_{c1} + R_{12}\mathbf{d}_2$ . This means that  $\mathbf{p}_c$  is a function only of  $\mathbf{y}$ . Now, since from the dynamical model we have

$$\begin{aligned} m_s \ddot{x}_c &= -\sin \theta_1 u_t \\ m_s \ddot{z}_c &= -\cos \theta_1 u_t + m_s \bar{g}, \end{aligned}$$

we can write  $u_t = m_s \|\mathbf{w}\|$  and  $\theta_1 = \text{atan2}(-w_z, -w_x)$ , where  $\mathbf{w} = \ddot{\mathbf{p}}_c - [0 \ \bar{g}]^T = [w_x \ w_z]^T \in \mathbb{R}^2$ , which is a function of  $\ddot{\mathbf{p}}_c(\ddot{\mathbf{p}}_{c1} \ \theta_{12}, \ddot{\theta}_{12}, \ddot{\theta}_{12})$ . Hence  $u_t = u_t(\ddot{\mathbf{p}}_{c1} \ \theta_{12}, \ddot{\theta}_{12}, \ddot{\theta}_{12})$  and  $\theta_1 = \theta_1(\ddot{\mathbf{p}}_{c1} \ \theta_{12}, \ddot{\theta}_{12}, \ddot{\theta}_{12})$ . Furthermore, from the last row of the system dynamics, we can write

$$\tau = \tau(\theta_{12}, \ddot{\mathbf{p}}_{c1}, \ddot{\theta}_{12}) = \beta^T(\theta_{12})\ddot{\mathbf{p}}_{c1} + m_B \ddot{\theta}_{12} + g_4(\theta_{12}).$$

Finally, using the third row of the system dynamics we have  $u_r = J_1 \ddot{\theta}_1 + \tau - d_{G_x} u_t$ , where after straightforward algebra  $\ddot{\theta}_1$  is function of  $(w_x, w_z, \dot{w}_x, \dot{w}_z, \ddot{w}_x, \ddot{w}_z)$ . This concludes the sketch of the proof.

### B. Sketch of flatness part of the Proof for Proposition 2, Case E

We recall the proposition 2 (Case-E) of Sec. IV of [1]:

**Proposition 2.** *The vector  $[\mathbf{p}_{c1}^T \ \theta_{12}]^T$  is an exactly linearizing output via dynamic feedback for the model with elastic-joint arm (Case-E), as long as  $u_t \neq 0$  and  $k_e \neq 0$ . As a consequence, they are also flat outputs.*

In order to possibly use the differential flatness property for planning purposes, we sketch the procedure to explicitly write down the algebraic map that relates  $\mathbf{y}, \dot{\mathbf{y}}, \mathbf{y}^{(3)}, \mathbf{y}^{(4)}$  with  $\theta_1, \dot{\theta}_1, \theta_{1m}, \dot{\theta}_{1m}$ , and  $\mathbf{u}$ . The position in  $\mathcal{F}_W$  of the CoM of the overall system can be written as in (4), which leads to  $u_t = m_s \|\mathbf{w}\| = u_t(\ddot{\mathbf{p}}_{c1} \ \theta_{12}, \ddot{\theta}_{12}, \ddot{\theta}_{12})$  and  $\theta_1 = \text{atan2}(-w_z, -w_x) = \theta_1(\ddot{\mathbf{p}}_{c1} \ \theta_{12}, \ddot{\theta}_{12}, \ddot{\theta}_{12})$  as in Sec. I-A. From the fourth row of the system dynamics we can write

$$\begin{aligned} \theta_{1m} &= \theta_{1m}(\theta_{12}, \ddot{\mathbf{p}}_{c1}, \ddot{\theta}_{12}) \\ &= \frac{\beta^T \ddot{\mathbf{p}}_{c1} + (m_B - J_m) \ddot{\theta}_{12} + g_4(\theta_{12}) + k_e \theta_{12}}{k_e}. \end{aligned} \quad (5)$$

The motor torque can be retrieved from the last row of the system dynamics using

$$\tau = \tau(\theta_{12}, \theta_{1m}, \ddot{\theta}_{1m}) = J_m \ddot{\theta}_{1m} + k_e \theta_{1m} - k_e \theta_{12},$$

where can  $\ddot{\theta}_{1m}$  be derived differentiating twice (5). The PVTOL torque can be retrieved from third row of the system dynamics as  $u_r = J_1 \ddot{\theta}_1 + \tau - d_{G_x} u_t$ , where  $\ddot{\theta}_1 = \ddot{\theta}_1(w_x, w_z, \dot{w}_x, \dot{w}_z, \ddot{w}_x, \ddot{w}_z)$ . This concludes the sketch of the derivation of the map for Case-E.

### C. Block Diagram of the Nonlinear controller

A block diagram of both the exact (dynamic feedback) linearizing and the outer loop controllers (presented in [1]) together with a smooth trajectory planner is provided in Fig. 1.

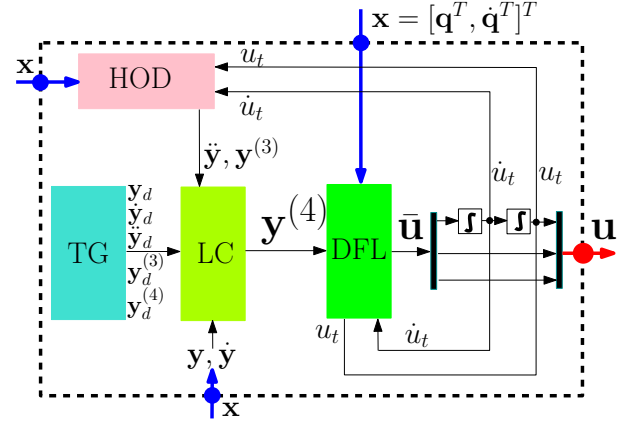


Fig. 1: Scheme of the exact linearizing controller. HOD stands for "High Order Dynamics", which analytically (i.e., exactly) computes the high order derivatives of the flat outputs  $\mathbf{y}$ , i.e.  $\dot{\mathbf{y}}$  and  $\mathbf{y}^{(3)}$  from the current state  $\mathbf{x}$ . TG, the "Trajectory Generator", generates the desired trajectory in  $C^3$ , based on a 4-th linear order filter. An outer loop "Linear Controller", LC, as in (14) of [1] controls the system brought in the linear form by the inner loop and tracks the desired outputs and their derivatives. DFL is the short form of "Dynamic Feedback Linearization" block, i.e., the inner loop which brings the system to the linear controllable form as in (2). Notice that everything inside the controller is framed with dashed line, and requires only the state of the system,  $\mathbf{x}$ , as input. The output of this overall control scheme,  $\mathbf{u} = [u_t \ u_t \ \tau]^T \in \mathbb{R}^3$ , is the control input entering to the system.

## II. EXTENSIVE AND REALISTIC SIMULATIONS

In the simulations, the nominal parameters of the system, their deviations, and the noise of the measured state are chosen close to the real values. A summary of the nominal values can be found in Table I. Deviation from the nominal values for mass, inertia and spring parameters are defined as percentages, while for distances are defined as offsets in proper units. Moreover, Gaussian noises with constant variances and zero biases in bandwidth between 10dB and 20dB are added to both position and velocity measurements. A summary of all deviation and noises are available in Table II. In all the simulation cases, the controller actions are computed using the nominal (i.e., wrong) values of the parameters and the noisy measurements. The system dynamics is instead integrated using the real values (i.e., nominal + deviations).

The noise variances for the velocity and angular speed measurement are chosen larger than for positions and orientation, respectively. For the measurements of the motor state we have chosen a smaller standard deviation than for the state of the PVTOL since servo motors generally provide good position/velocity estimation with high resolution encoders.

The system dynamics is simulated with Simulink at 1 KHz. The positions and velocities are provided at a rate of 30Hz, to the controller, similarly to what a commercial camera+IMU setup would provide. All orientations and angular velocities are given at 500 Hz, which is a realistic value both for IMU attitude estimation and motor encoder readings.

In the dynamic models, the link attached to PVTOL is considered as a rod, whose inertia is computed using  $J_2 = m_2 L^2 / 12$ , where  $L = \|\mathbf{d}_2 + \mathbf{d}_e\|$ . The motor inertia is computed as  $J_m = g_r^2 J_{ms}$  where  $g_r$  is its gear reduction ratio, where

$J_{ms} = m_r r_r^2 / 2$  is calculated by considering motor as a rotating solid cylinder.

The stiffness range of the elastic actuator is chosen similar to the one from [7]. Physical limits to all actuators are considered as hard thresholds, as given in Table I.

In the plots of the simulations (see Figs. 3-6), for *nominal values* we mean the system behavior in the ideal case, i.e., as if the controllers were fully aware of the real parameters (nominal + deviation) of the system dynamics and there was neither noise nor under-samplings in the measurements. The *actual values* represent instead the system behavior when the controllers use the nominal (thus wrong) parameters and the measurements are under-sampled and noisy.

For numerical validation, two important scenarios are considered; *i)* aerial grasping, and *ii)* link velocity amplification. It is observed that the rigid-joint design is more suitable for the first scenario, while using an elastic-joint arm is much more advantageous for the second one.

Furthermore, we tested our controller in a simulation considering the full dynamical 3D model of the system, using the CAD model of the experimental setup in Sim-Mechanics, which is known to be a realistic physical simulation toolbox provided by Matlab. Our 3D system consist of a quadrotor equipped with a Qbmove VSA [7], which is also connected to a rigid arm (see Fig. 3 of [1]). We split the 3D model into two planes, Plane-A and Plane-B as shown in Fig. 3a of [1]. All the motion on Plane-A (including that of the absolute link angle) is controlled using the exact linearizing controller presented in Sec. III of [1] (via thrust, torque around  $\mathbf{x}_1$  and torque for the Qbmove VSA, see Fig. 1). The rest of the quadrotor motion (motion in Plane-B – except the translation along  $\mathbf{z}_1$  – and rotation around the vertical axis  $\mathbf{z}_1$ ) is controlled using a *near-hovering controller*, which is explained in [8]. This allows us to test the performance of the controller presented in [1] in a real experimental scenario. The controllers are tested together with the CAD model of the real setup in SimMechanics, and the results are given in the video attachment of [1].

#### A. Aerial Grasping

The first set of simulations is aimed at testing the grasping of a stationary object using the arm both for Case-R and Case-E. The grasped object mass is denoted with  $m_o > 0$ . At time  $t_g$  (grasping time instant) mass  $m_o$  is attached to point  $P_E$ . The effect of grasped mass to the system is accurately dynamically modeled as following

- The mass of arm is updated to  $m_{2_{t \geq t_g}} = m_2 + m_o$ ,
- The distances  $\mathbf{d}_2$  and  $\mathbf{d}_e$  are updated using the formulas

$$\begin{aligned} \mathbf{d}_{2_{t \geq t_g}} &= \mathbf{d}_2 + \mathbf{d}_e \\ \mathbf{d}_{e_{t \geq t_g}} &= \mathbf{d}_e - \mathbf{d}_e \end{aligned}$$

where  $\mathbf{d}_e = \frac{m_o}{m_{2_{t \geq t_g}}} \mathbf{d}_e$ ,

- Using parallel axis theorem, the link inertia is updated to

$$J_{2_{t \geq t_g}} = \frac{m_{2_{t \geq t_g}}}{12} L^2 + m_{2_{t \geq t_g}} \|\mathbf{d}_e\|^2.$$

where  $L = \|\mathbf{d}_2 + \mathbf{d}_e\|$  as before.

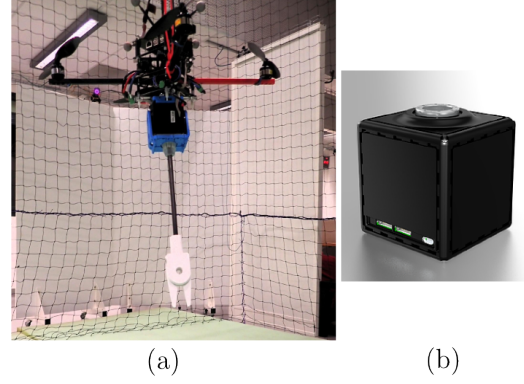


Fig. 2: (a) Picture of the experimental setup tested in [1], together with a 3D printed gripper at the end of its arm. A Qbmove VSA is attached to the quadrotor.

(b) Close up on the Qbmove VSA more details can be found at <http://www.naturalmachinemotioninitiative.com>.

Moreover, due to differences between the end-effector and the stationary mass velocities, an impact will occur at the moment of grasping. The external force to the system will be then

$$\mathbf{f}_{ext} = \mathbf{J}^T \mathbf{f}_{imp}$$

where

$$\mathbf{f}_{imp} = -m_o \frac{\dot{\mathbf{p}}_e - \dot{\mathbf{p}}_o}{T_i}$$

with end-effector velocity  $\dot{\mathbf{p}}_e$  is computed as time derivative of

$$\mathbf{p}_e = \mathbf{p}_{c1} + \mathbf{R}_{12}(\mathbf{d}_2 + \mathbf{d}_e)$$

and stationary object velocity is  $\dot{\mathbf{p}}_o = \mathbf{0}$ . The interval  $T_i$  represents the impact duration and its value is given in Table I. The jacobian matrix  $\mathbf{J}$  is different for the rigid-joint arm and the elastic-joint arm cases. For the former it is

$$\mathbf{J} = \begin{bmatrix} 1 & 0 & 0 & \cos(\theta_{12})(d_{2z} + d_{ez}) - \sin(\theta_{12})(d_{2x} + d_{ex}) \\ 0 & 1 & 0 & -\cos(\theta_{12})(d_{2x} + d_{ex}) - \sin(\theta_{12})(d_{2z} + d_{ez}) \end{bmatrix}$$

and for the latter it is

$$\mathbf{J} = \begin{bmatrix} 1 & 0 & 0 & \cos(\theta_{12})(d_{2z} + d_{ez}) - \sin(\theta_{12})(d_{2x} + d_{ex}) & 0 \\ 0 & 1 & 0 & -\cos(\theta_{12})(d_{2x} + d_{ex}) - \sin(\theta_{12})(d_{2z} + d_{ez}) & 0 \end{bmatrix}.$$

A composite trajectory is chosen in which an object with  $m_o = 0.5\text{kg}$  is grasped by the end-effector at time instant  $t_g = 2.67\text{s}$ . At this instant the joint arm is at its maximum orientation from an initial condition, the PVTOL is at a high velocity in  $+\mathbf{x}_W$  direction and at the beginning of its raising up along the  $-\mathbf{z}_W$  axis (remember that  $+\mathbf{z}_W$  is facing down). In all cases the desired trajectories have different initial values from the actual starting configuration of the system, so that we can test also the convergence capabilities of the controller in the transient phase in addition to the tracking ability.

1) *Grasping with Rigid-joint Arm:* The results are given in Fig. 3. Two cases are compared: known grasped mass (k.m.) vs. unknown grasped mass (u.m.). After the grasping moment  $t_g$ , the deviations from desired trajectories can be clearly seen for both cases. If the grasped mass is unknown, such deviation is higher for all flat outputs. In the nominal case (see yellow solid curve in Fig. 3) controller is fully aware of its velocity

Quantities	Notation	Nominal Value or Range	Unit
PVTOL mass	$m_1$	1.00	kg
motor mass	$m_m$	0.20	kg
link mass	$m_2$	0.30	kg
rotating motor mass	$m_r$	0.05	kg
object mass	$m_o$	0.5	kg
PVTOL inertia	$J_1$	0.028	kgm <sup>2</sup>
motor solid inertia	$J_{ms}$	0.0562e-06	kgm <sup>2</sup>
motor inertia	$J_m$	0.4101	kgm <sup>2</sup>
link inertia	$J_2$	0.004	kgm <sup>2</sup>
dis. vec. betw. $P_{C_2}$ & $P_M$	$\mathbf{d}_2$	$[0 \ 0.2]^T$	m
dis. vec. betw. $P_{C_2}$ & $P_E$	$\mathbf{d}_e$	$[0 \ 0.2]^T$	m
dis. vec. betw. $P_{C_1}$ & $P_G$	$\mathbf{d}_G$	$[0.01 \ 0.05]^T$	m
motor shaft radius	$r_r$	0.015	m
linear spring stiffness	$k_e$	$8 \leftrightarrow 30$	Nm/rad
motor gear ratio	$g_r$	270:1	-
PVTOL thrust range	$T_l$	$0.1 \leftrightarrow 28$	N
PVTOL torque range	$T_r$	$-3 \leftrightarrow 3$	Nm
Motor torque range	$T_m$	$-5 \leftrightarrow 5$	Nm
grasping time	$t_g$	2.67	s
impact duration	$T_i$	0.01	s

TABLE I: Summary of the nominal parameters of the simulations.

Non-idealities	Notation	Value	Unit
deviation in masses	$\delta_m$	2	%
deviation in inertias	$\delta_i$	10	%
deviation in $\mathbf{d}_2$	$\delta_2$	$[0 \ 0.01]^T$	m
deviation in $\mathbf{d}_G$	$\delta_G$	$[0 \ 0.01]^T$	m
deviation in spring constant $k_e$	$\delta_s$	5	%
3-sigma Gauss. noise in pos.	$3\sigma_p$	0.01	m
3-sigma Gauss. noise in vel.	$3\sigma_v$	0.02	m/s
3-sigma Gauss. noise in $\theta_1$	$3\sigma_1$	0.01	rad
3-sigma Gauss. noise in $\theta_1$	$3\sigma_{d1}$	0.02	rad/s
3-sigma Gauss. noise in $\theta_2, \theta_m, \theta_e$	$3\sigma_2$	0.001	rad
3-sigma Gauss. noise in $\theta_2, \theta_m, \theta_e$	$3\sigma_{d2}$	0.002	rad/s

TABLE II: Summary of the deviations from nominal parameters and noise levels used in the simulations. Deviations in masses, inertias and spring parameters are considered as a percentage, while for distances they are offsets. The controllers in each simulation are not aware of these deviations. Moreover, noises are added to each measurement, whose standard deviations are reported in the table.

and the object mass, hence it generates high peaks in torques to counterbalance the impact. For the actual cases (see red and pink solid curves in Fig. 3) the controller is aware of the model with some deviations, hence it produces less reaction to impacts compared to nominal case, which results in a worse tracking performance.

2) *Grasping with Elastic-joint Arm*: Two cases are compared: grasping with low stiffness spring,  $k_e = 8$  Nm and with high stiffness spring,  $k_e = 30$  Nm. Results are given in Fig. 4, this time together with the actual absolute motor orientation  $\theta_{1m}$  depicted with purple dashed curves. In both the low and high stiffness cases, the tracking performance of the flat outputs are very close to each other, moreover it is very similar to the results given in Fig. 3, with a clear difference in the absolute link orientation  $\theta_{12}$ . However, the cost of it is the control effort, that is much more for Case-E than for Case-R. Using high stiffness joint mitigates this effect and results beneficial for the aerial grasping task. In fact in our simulations we found that for  $k_e = 50$  Nm/rad a stable grasping has been performed within the physical limits of the

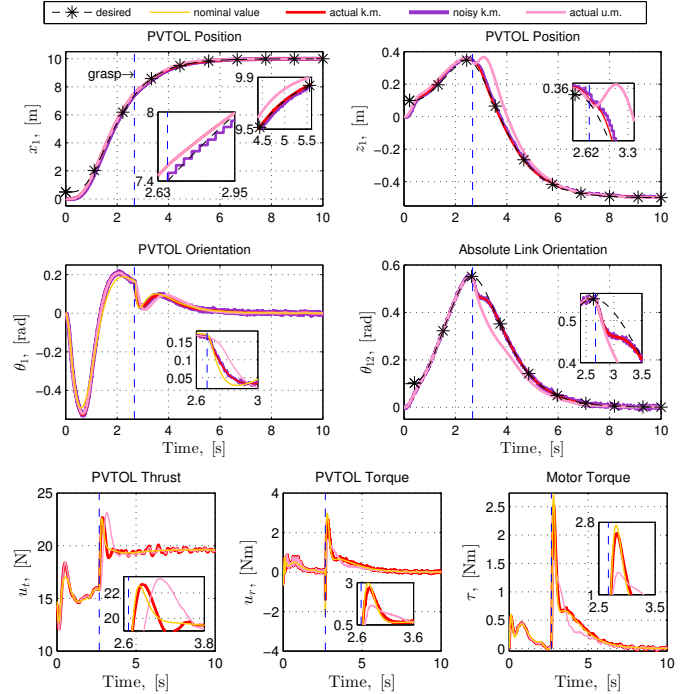


Fig. 3: Aerial grasping with PVTOL+rigid-joint arm. The desired trajectory is depicted with a black dashed curve. The grasping moment is  $t_g = 2.67$ s (shown with a vertical dashed line). The nominal signals are plotted with yellow solid curves. In the case of known grasped mass (k.m.), the actual values and the noisy measurements (entering to the controller) are presented with red and purple solid curves, respectively. The pink solid curve is used for the case of unknown grasped mass (u.m.). Notice that gravity is along the  $+z$  direction. The small figures are the magnified plots of the individual subfigures at around the grasping moment.

actuators (no overshoots in torques). In this case is however possible to see a less performant tracking of  $\theta_{12}$ . We did not put these supplementary results in this report for brevity. Finally, one can conclude this simulation set saying that for aerial grasping task and for tracking a generic trajectory Case-R is more advantageous than Case-E.

### B. High-speed Oscillations: Link Velocity Amplification

In this section we present a second simulation set in which the elastic-joint arm is more beneficial than a rigid-joint arm configuration. We consider a scenario, where the link is asked to oscillate at high velocities, which could be used for tasks such as hammering on a surface or throwing an object far away. Such case was studied before by the authors, where a light-weight elastic-joint arm was developed and its link velocity was amplified w.r.t. the motor velocity, and experimental results have been provided in [9]. However, the controller for flying robot presented in that work was a near hovering approximate linearization controller and it did not exploit the exact feedback linearization and flatness properties of the system.

Here we perform a similar link velocity amplification task, using the controller presented in Section IV of [1]. We choose  $k_e = 8$  Nm/rad for the simulation. The natural frequency of the system is identified by setting the gravity to zero and

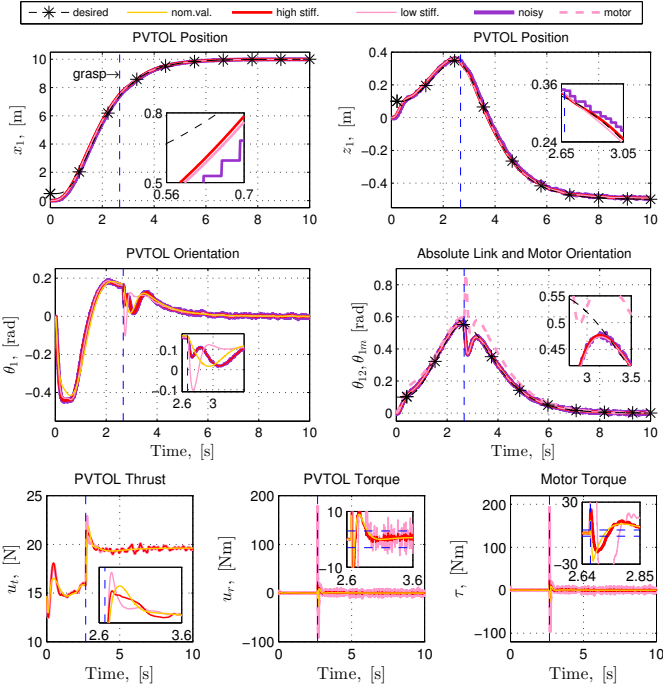


Fig. 4: Aerial grasping with PVTOL+elastic-joint arm. The desired trajectory is depicted with black dashed curve. The grasping moment  $t_g = 2.67$ s is shown with a vertical dashed line. The nominal values for high stiffness case are given with yellow solid curves. The red solid curve stands for the actual signals for the high stiffness joint simulation, and pink solid curve depicts the actual values of the low stiffness joint simulation. The pink dashed curve shows the absolute motor orientation only in the plot on the second row and second column. Physical limits on torques are shown with blue dashed horizontal lines.

letting the arm evolve freely from an initial condition of 60 deg and observing its behavior. We found that for nominal values, arm swings with period of  $T = 0.255$ s. We used this value to generate the frequency of the desired trajectory for  $\theta_{12}$  with a constantly increasing amplitude until a certain constant value. We also set the desired trajectory of the position constantly at zero.

Results of Case-E are reported in Fig. 6 shows a good position tracking performance, with less than 1 cm of maximum error. Link and motor velocities are given in third subfigure of the first column, where link velocity is amplified of more than five times w.r.t. the motor velocity. Notice that the PVTOL and motor torques are saturated in order to simulate the physical limits, which is the reason of the small tracking errors.

Results for Case-R are reported in Fig. 5. Here the tracking performance is even better than Case-E. However this is achieved only due to the violation of the PVTOL and motor torque limits, and they reach very high values. In fact, in our simulations, saturating the torques to their physical limits for Case-R has always ended up with an unstable behavior for tracking such high-speed trajectory.

Despite the hard physical limits applied for the Case-E, requested link velocity is achieved and much less control effort has been used when compared to Case-R. The reason for this is the ability of storing energy in the elastic components. This implies that Case-E has more advantages than Case-R for the

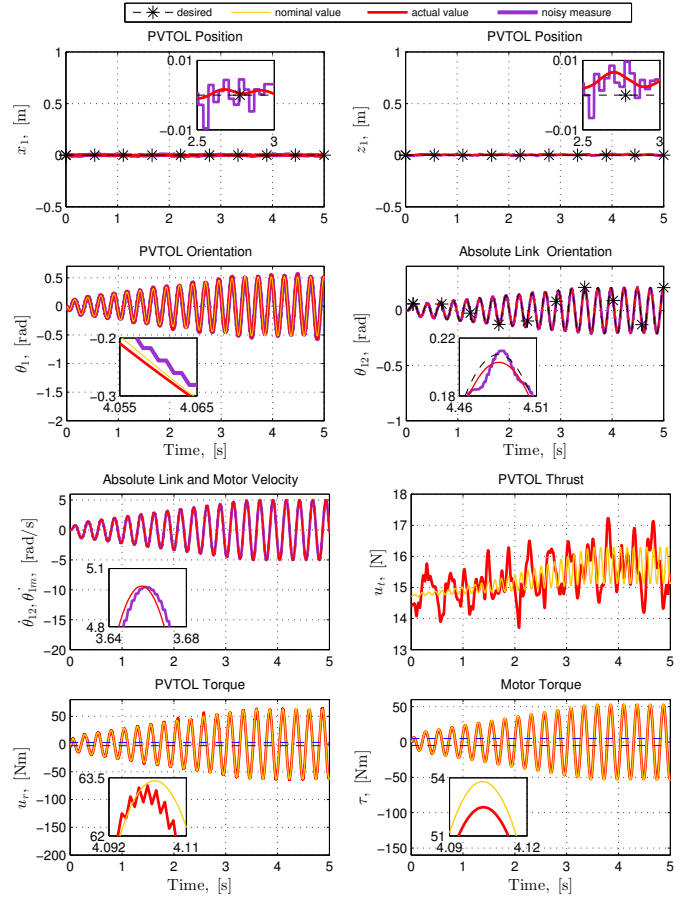


Fig. 5: Oscillating at high link speed in the case Case-R. The desired trajectory profile is depicted with a black-dashed curve. The yellow solid curves stand for the nominal signals, the red solid curves for the actual signals, and the purple solid curve for the noisy measurements of the actual values (entering to the controller). The blue dashed horizontal lines present the physical limits of the PVTOL and motor torques which, if enabled, would cause instability of the system.

tasks that require high link speed, such as, e.g., throwing or hammering.

### III. TOWARDS AERIAL PHYSICAL EXPERIMENTS

A deep study on control of an aerial vehicle equipped with an elastic-joint arm is presented in [1]. There we also present the preliminary results of the controller using the experimental setup, which consist of a quadrotor VTOL and Qbmove VSA (Variable Stiffness Actuator) [7]. Here we provide a description of the overall system provided with a gripper at the end of the arm (see Fig. 2).

Let us now describe in detail the preparation of the Qbmove VSA in for our experimental setup. Recall that Qbmove VSA, is an agonistic/antagonistic servo-VSA. Shortly, it consists of two *PD* controlled servo motors, which allow to regulate independently desired stiffness and output-shaft equilibrium, i.e., in our notations  $k_e$  and  $\theta_m$ , respectively. This VSA (see Fig. 2) provides state measurements  $(\theta_m, \theta_e)$  at 500Hz. In order for our controller to work with Qbmove VSA, several extra steps

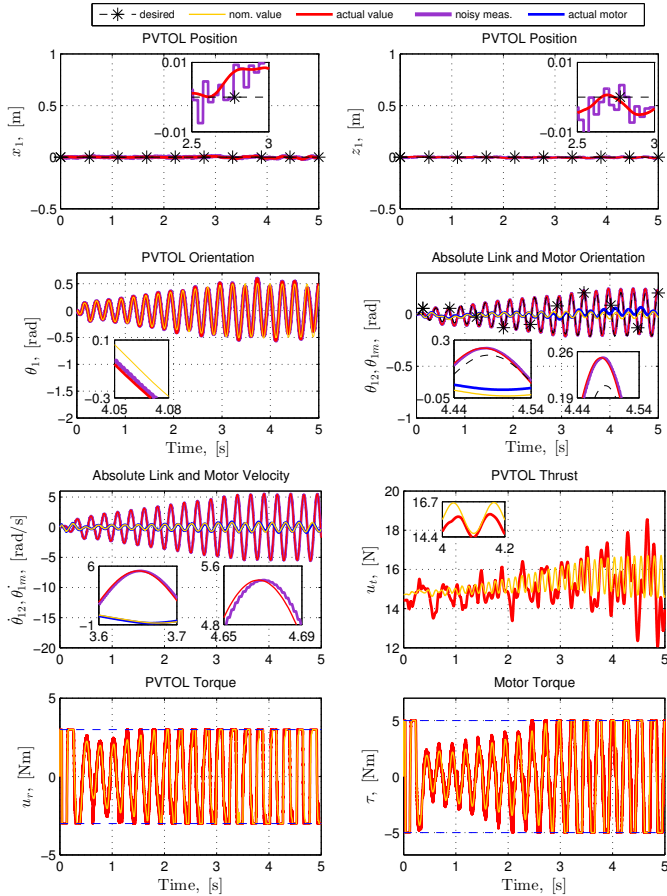


Fig. 6: Link velocity amplification is obtained in the Case-E. The desired trajectory profile is depicted with black-dashed curve. The yellow solid curves stand for the nominal signals, the red solid curves for the actual signals, and the purple solid curve for the noisy measurements of the actual values (entering to the controller). The blue solid curve presents the motor values ( $\theta_{1m}, \dot{\theta}_{1m}$ ) and are shown together with link values ( $\theta_{12}, \dot{\theta}_{12}$ ) in the same subplots. The blue dashed horizontal lines present the physical limits of PVTOL and motor torques, which in this case, contrarily to Case-R, can be enabled without mining the stability of the system.

need to be conducted. First of all, a parametric identification of the Qbmove VSA + rigid arm system has been performed, in order to retrieve the parameters of the equivalent motor studied in [1]. The stiffness (and the damping) parameters of the Qbmove+arm system are identified by first assuming it as a simple mass-damper system, and then letting the arm swing from an initial condition, without any control action (see [9] for similar a method). Note that the Qbmove features a nonlinear spring, we consider a linear spring for deflection in the range of  $\pm 20$  deg. Inertial parameters of the system are found using the system geometry. Moreover, the control framework we presented requires a torque-controlled motor, while a Qbmove is not proposing this control modality. For this reason we have implemented an outer loop controller around the Qbmove device, which translates the desired torque into a desired position through a feedback linearization scheme. This approach requires a precise knowledge of the system parameters; distances, masses and inertia were computed through CAD model, while other parameters were experimentally

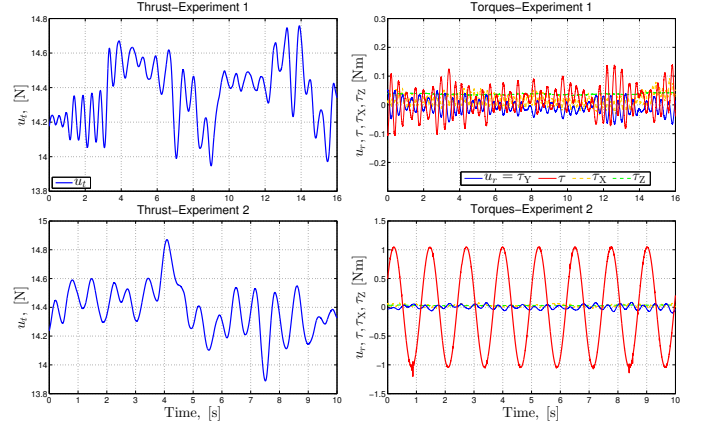


Fig. 7: Control inputs of the system for the two experiments presented in [1]. The first row corresponds to the results given in Fig. 4, and the second row to that of Fig. 5 of [1].

identified as described above (all these parameters are given in Table III of [1]). For this reason we also implemented an outer loop controller around the Qbmove device, which translates the desired torque into a desired position using the estimated parameters and second order system model. This *bridge* between the proposed controller of [1] and the Qbmove VSA is directly implemented as a ROS node. We avoid the details on this part for the sake of brevity.

At last, we also display the control inputs in the case of two experiments described in [1]. In Fig. 7, the first and second rows show the control inputs for the first and second experiment, respectively.

#### IV. ACKNOWLEDGEMENTS

We thank Anthony Mallet (LAAS-CNRS) for his contribution in the software architecture of the experiments.

#### REFERENCES

- [1] B. Yüksel, N. Staub, and A. Franchi, “Aerial robots with rigid/elastic-joint arms: Single-joint controllability study and preliminary experiments,” in *2016 IEEE/RSJ Int. Conf. on Intelligent Robots and Systems*, Daejeon, South Korea, Oct. 2016.
- [2] A. Isidori, *Nonlinear Control Systems*, 3rd edition. Springer, 1995.
- [3] P. Martin, R. M. Murray, and P. Rouchon, “Flat systems, equivalence and trajectory generation,” in *2003 CDS Technical Report*, 2003.
- [4] A. De Luca and G. Oriolo, “Trajectory planning and control for planar robots with passive last joint,” *The International Journal of Robotics Research*, vol. 21, no. 5-6, pp. 575–590, 2002.
- [5] M. Fliess, J. Levine, P. Martin, and P. Rouchon, “A Lie-Bäcklund approach to equivalence and flatness of nonlinear systems,” *IEEE Trans. on Automatic Control*, vol. 44, no. 5, pp. 922–937, 1999.
- [6] J. Thomas, J. Polin, K. Sreenath, and V. Kumar, “Avian-Inspired Grasping for Quadrotor Micro UAVs,” in *2013 ASME Int. Design Engineering Technical Conf. and Computers and Information in Engineering Conf.*, Portland, OR, Aug. 2013.
- [7] QB-ROBOTICS, “Variable Stiffness Actuator,” <http://www.qbrobotics.com/>.
- [8] D. J. Lee, A. Franchi, H. I. Son, H. H. Bühlhoff, and P. Robuffo Giordano, “Semi-autonomous haptic teleoperation control architecture of multiple unmanned aerial vehicles,” *IEEE/ASME Trans. on Mechatronics, Focused Section on Aerospace Mechatronics*, vol. 18, no. 4, pp. 1334–1345, 2013.
- [9] B. Yüksel, S. Mahboubi, C. Secchi, H. H. Bühlhoff, and A. Franchi, “Design, identification and experimental testing of a light-weight flexible-joint arm for aerial physical interaction,” in *2015 IEEE Int. Conf. on Robotics and Automation*, Seattle, WA, May 2015, pp. 870–876.